Detecting Crystals in Suspensions: Convolutional Neural Networks vs. Gravity-Based Approach for Size Distribution Detection

Laura Neuendorf, Stefan Höving, Lennard Bennemann, and Norbert Kockmann*

DOI: 10.1002/cite.202200235

The majority of fine chemical and pharmaceutical processes includes some form of crystallization steps. For process optimization and control of further downstream steps, the crystal size distribution of the product is a crucial factor. To identify characteristic particle size classes from a large number of measurements, each individual probe has to be separated from the mother liquor and manually analyzed. In this contribution a deep learning-based method is presented using microscopic images as input for crystal size analysis. Additionally, a data augmentation approach was investigated to limit the data necessary for learning. A high segmentation accuracy of the crystals was achieved with 93.02 %. To evaluate the classification performed by the presented convolutional neural network (CNN), it is tested on two sets of images, containing a previously determined particle fraction. With the classifications of the CNN, a Q_3 distribution is calculated. To validate the developed approach in terms of its accuracy it is compared to two other methods as well.

Keywords: Computer vision, Continuous cooling crystallization, Convolutional neural networks, Draft tube baffle crystallizer, Particle size distribution

Received: December 16, 2022; *accepted:* April 26, 2023

1 Introduction

Crystallization is used at least once in the production of a solid product [1]. Additionally, crystallization processes are of increasing interest in the chemical industry [1–3]. To monitor the crystallization properly, the particle size distribution (PSD) is a useful and common key parameter [4]. It is conventionally determined using sedimentation analysis or sieving techniques [5]. More elaborated techniques make use of laser technologies, especially laser diffraction [6, 7]. However, with increasing availability of high-resolution cameras, digital image processing routines or computer-vision based approaches, where images of particles are evaluated to determine the PSD, gain importance since twenty years [8–10]. A rising trend of vision-based measurement, so-called visual sensors, is observable [11] due to this development. In the field of crystal analysis, image evaluation made a huge progress as well, developing from extensive personal examinations under the microscope to the implementation of cameras, replacing the human observation [1]. Schmalenberg et al. [12, 13] proposed a semi-automatic approach, based on the method established by Borchert et al. and modified with the method established by Huo et al. [13–15].

The approach of Schmalenberg et al. is time-consuming due to the manual actions still necessary [13]. Therefore, in this paper an approach is presented to determine the PSD using an algorithm based on artificial intelligence (AI). Since the AI-based algorithm works almost automatically after generating the training data and determining the optimal parameters, the time required and thus the sensing costs are reduced, especially when the AI-based approach is used frequently. Another advantage is the non-invasive measurement of the PSD, even though it is an inline measurement method.

2 Material and Methods

2.1 Experimental Setup

To analyze crystals, images of the crystals have to be taken. The following setup of a tube crystallizer, build by Schmalenberg et al., is used for this purpose, see Fig. 1 [16].

[1]Laura Neuendorf‡ https://orcid.org/0000-0001-6593-1752,
[1]Stefan Höving‡, [1]Lennard Bennemann,
[1]Prof. Dr.-Ing. Norbert Kockmann
(Norbert.kockmann@tu-dortmund.de)
[1]TU Dortmund University, Department of Biochemical and Chemical engineering, Laboratory of Equipment Design, Emil-Figge-Straße 68, 44227 Dortmund, Germany.
‡ These authors contributed equally.

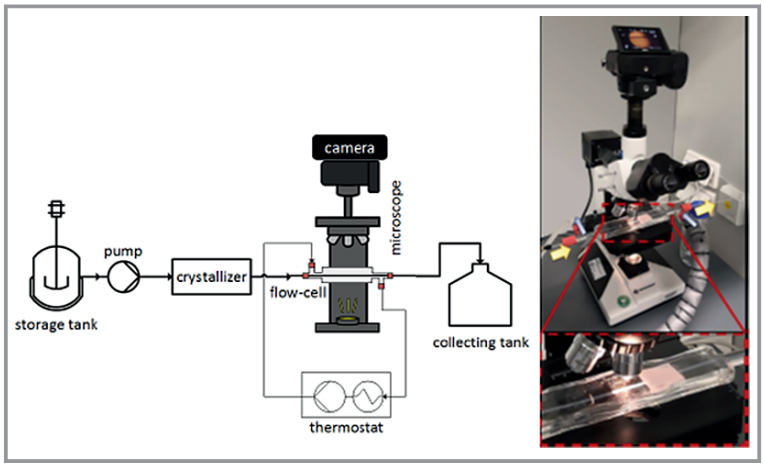

Figure 1. Scheme of the experimental setup (left), photo of the microscope and the camera in the setup (upper right), photo of the flow cell under the microscope (lower right).

The relevant part for image acquisition is the flow cell located below the microscope. The crystals are passed in a suspension through a fluorinated ethylene-propylene (FEP) tube (inner diameter $d_i = 1.6$ mm and outer diameter $d_o = 3.2$ mm, Bohlender GmbH, Grünsfeld, Germany). This tube is guided through a flow cell made of glass (crafted by glassblowing workshop from TU Dortmund University). The images are obtained by the camera (Z6, Nikon, Japan) mounted above the microscope.

As shown in the more detailed image in Fig. 1 (right image), the flow cell is located under a microscope. To minimize the interference of the tubing, the flow cell is filled with water, because water and FEP have a similar refractive index (FEP: 1.3380–1.344 [17]; water: 1.3312–1.3372 [18]). Since this experiment is only for evaluation purposes, the setup is fed with a suspension containing crystals with a known PSD (*L*-alanine/water solution at room temperature, prepared with defined solid crystals (1 wt %; purity ≥ 99.6 %, Evonik Rexim (Nanning) Pharmaceutical Co., Ltd, China). Those crystals were sieved after being dry-pestled to obtain defined particle size fractions (90–125 µm; 125–180 µm). Therefore, the crystallizer is just used as an additional tube and not as a crystallizer. The other parts from the experimental setup are not important for the acquired images and are not further examined. For the interested reader, more information can be found in [13, 16, 19, 20].

2.2 Convolutional Neural Networks

A method to implement machine learning (ML) inspired by biological neural networks are artificial neural networks (ANN). Convolutional neural networks (CNNs) are a subgroup of ANNs, especially designed for processing data with a grid-like topology, such as images [21]. ANNs consist of so-called artificial neurons, functions that calculate an output from several weighted inputs. Deep learning (DL) deals with neural networks that consist of several layers of neurons and are therefore referred to as deep [21].

After the CNN architecture is defined, the model must be trained to be used as a classification tool. That is achieved in the training step, where the different model parameters are updated by a forward-backward propagation. Different parameters such as number of convolutional layers, number of FCL neurons and others detailed are updated by feeding a set of labeled images to the CNN model, referred as the training dataset [22, 23].

Images from the training dataset are fed to the CNN model, and the error is computed by comparing the predicted image operation state with the manually labeled one. This process is repeated several times and the error, or loss, is minimized through a gradient descent approach. After multiple iterations, this process is interrupted, and the model can be used as a predictive tool [22].

The CNN model's predictive accuracy is assessed from a validation dataset. This set of labeled data is similar to the training dataset, but it is not used during the training step. Hence, the validation dataset can be interpreted as unseen information data by the CNN model. In order to compute the validation accuracy, the CNN inferred operation states from the validation images are compared against the manually labeled data. As observed, the accuracy and predictive power of a CNN model is heavily dependent on the CNN architecture, as it will be detailed in the next section [22].

2.3 Employed Neural Network

In order to determine the PSD by CNN, a suitable CNN must be trained first. To save time, instead of training the network from the scratch, the network will be trained by transfer learning. Taylor and Stone show that transfer learning saves time and still gives good results [24]. As a pretrained network, ResNet-50 prevailed over other networks such as ResNet-18 and ResNet-34. A bigger network has an increased computational effort but also an increased accuracy [11].

2.4 Particle Size Distribution

As stated by Stieß, the PSD is an important characteristic for solids [25]. The PSD can be expressed in different ways, each related to a different dimension. To compare between different methods, a volume-related distribution is chosen. Typically, only single crystals and no agglomerates are considered for evaluation as a PSD. Therefore, agglomerates

(or overlapping crystals) are unwanted in the detection. Since agglomerates and overlapping crystals cannot be distinguished from each other they are treated the same way. Both usually exhibit a lower circularity value than single crystals, thus a threshold can be applied in the detection. While agglomerates usually lie in the range of about 50–85 %, crystals are more in the range of 85–95 %. However, some agglomerates or overlapping crystals with a high circularity, as defined in Eq. (1) might still be misdetected as crystals.

$$f_{\mathrm{circ}} = \frac{4\pi A}{P^2} \tag{1}$$

The shape factor circularity f_{circ} is defined as 4π times the area A divided by the squared perimeter P of the shape [26]. For an ideal circle the value is equal to 1.

This cumulative distribution sum Q_3 represents the volume proportion of particles in a specific diameter range in the total volume quantity. The determined particle size diameter will be estimated as circular area equivalent diameter. To model the measured PSD a logarithmic normal distribution (LND) is applied. Eq. (2) shows the computation of the volume related cumulative distribution Q_3, using the error function *erf*, particle size diameter x, volume related mean particle size diameter $x_{50,3}$ and the standard deviation σ_{LND}.

$$Q_3(x_i) = \frac{1}{2}\left[1 + erf\left[\frac{ln\left[\frac{x_i}{x_{50i}}\right]}{\left[\sqrt{2}\,\sigma_{\mathrm{LND}}\right]}\right]\right] \tag{2}$$

In Eq. (1) x_{50}, later also described as $x_{50,3}$, refers to the diameter of the particle, which cumulated volume marks half of the total volume. The parameter σ_{LND} describes the log normal distribution standard aberration and therefore a factor that should be minimized. Further, σ_{LND} describes the sum of the quadric deviation of the estimated distribution and the experimental data.

3 Semantic Segmentation of Crystals

In the following, the developed methodology for the segmentation of images of crystals in the flow cell is presented. Semantic segmentation means pixel-wise classification based on convolutional networks is used. In addition, the investigated AI metrics are explained in detail.

3.1 Semantic Segmentation Metrics

Several metrics for the performance of a neural net are available. To obtain further insights about incorrectly classified pixels in images accuracy as a metric can be applied. To use it the terms true positives t_p, where positive cases are identified as positive, true negatives t_n, where negative cases are identified as negative, false positives f_p, where negative cases are identified as positive, and false negatives f_n, where positive cases are identified as negative need to be introduced. Then the accuracy is defined as [21, 23]:

$$Accuracy = \frac{t_p + t_n}{t_p + t_n + f_p + f_n} \tag{3}$$

In order to determine the PSD of the microscopic images a suitable CNN must be trained first. Since the size of the crystals is of important matter, the CNN will classify each pixel of an image in one of three categories: black background, light background and crystal. The crystal is a region of interest (ROI), which is identified by the CNN.

3.2 Training of Network and Data Augmentation

To train the network, sufficient training data is required. Here, 525 images with a size of 224 × 224 pixels from more than ten different experiments of various substance classes of Schmalenberg et al. were used as training data set [13]. At first, the so-called image labeling is performed manually using MATLAB's built-in image labeling tool. In this approach, every pixel is manually assigned to one of three classes. The three categories are black background, light background and crystal as seen in Fig. 2.

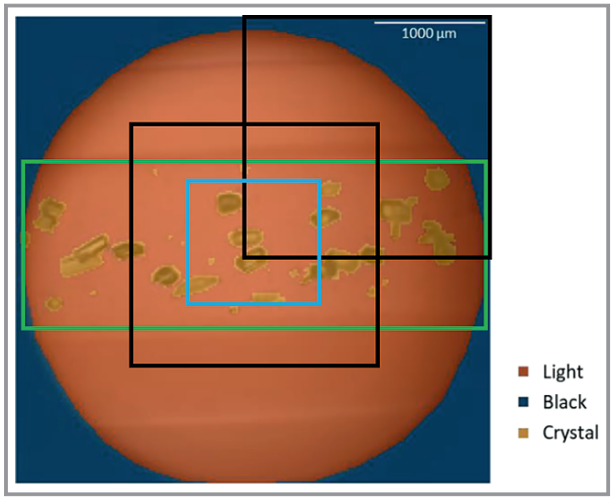

Figure 2. Labeled image in the Matlab image Labeler, consisting of three classes, light (orange) and black background (dark blue) and crystals (yellow). Moreover, the cut sections are indicated.

Fig. 2 displays a labeled image for training of the type "central section cut out". The images are cropped so that the illuminated circle determines the image border. Other types of cropping the data set, including cropping out a central or cornered quarter (indicated by black box) or a squared section of it (indicated by blue box). Their respective amount in the training data is detailed in Tab. 1. The green box indicates the final image section where the results

Table 1. The division of training images into their preprocessing and the method they are cut.

Type of image cropping	Amount [–]
Whole image	138 plus 9 as validation
Central quarter	75
Cornered quarter	88
Central only lens square	224

evaluation was performed. It shows the central area with the brightest illumination.

By not only using the central sections, but also cropped sections of it, more percent of the image belonged to the class crystal. Also, accuracy could be improved by excluding dark background with the "central only lens square" cut, because sometimes it was detected as crystals. However, these improvements were just added to the overall training amount, so the original centrally cut section remained in the training data. After labeling, it was counted in pixels how much the different classes are represented in the training data, see Tab. 2. The "Pixel Count" of every class is divided by the respective "ImagePixelCount". The ImagePixelCount additionally counts the number of pixels in images that have an instance of the class. The result is the frequency of every class. To extract class weights out of this information, the median of the frequency is divided by the frequency of every class.

When the images are labeled, it is advisable to apply weights to the training layers to improve the recognition of a less dominant class. Without weights, the CNN restructures itself most for the dominant classes. The background takes the most shares of the training images, as seen in Tab. 2, but the crystals are the desired class. Since the crystals as the ROI are underrepresented compared to the background, measured by pixel count and resulting frequency, weights are applied to the training layers. Their values are set so that the classes become equally important.

To reduce the risk of overfitting, where the network can no longer generalize to new unseen image data, the data augmentation settings listed in Tab. 3 were used during training [27]. Moreover, data augmentation improves the translation invariance, which means that the network becomes more robust to localization changes of the desired objects in the images [28].

Table 3. Data augmentation settings during CNN training.

Data augmentation technique	Set value
Random *X* reflection	applied
Random rotation	0–90°
Random *X* shearing	0–45°
Random *Y* shearing	0–45°
X Translation [pixel]	–100 to 100
Y Translation [pixel]	–100 to 100
Zoom	0.75–150

Several training runs were performed as pretest; however the most promising result were obtained by using the following settings for Resnet-50: a training length of 500 epochs and a mini batch size of eight. Shorter training or smaller mini batch size led to lower accuracy during the training. Larger training length led to worse validation accuracy, meaning the net's ability to correctly detect unseen images decreased. Larger mini batch size did not improve accuracy, however led to longer training duration. Larger values applied in data augmentation, as well as smaller also led to decreasing training and validation accuracy during training.

The final training course of the network is displayed in Fig. 3. The obtained accuracy for training data (blue curve) and validation data (black curve) is shown. The training accuracy, the number of correctly classified pixels in an image, reaches values of around 90–95 % per iteration during training. The final validation accuracy reached 93.02 %.

As usual in training a neural net, validation accuracy is lower than training accuracy. This is because the validation data set of labeled data is not used during the training step. Hence, the validation dataset can be interpreted as unseen information data by the CNN model. So, the validation accuracy describes that the CNN can generalize to unseen crystal images.

3.3 Results of the Neural Net

The resulting CNN classifies all pixel of an image unknown to the network as shown in Fig. 4. The bright blue color in-

Table 2. The counted pixels assigned to each class, their frequency and the resulting weights of the three classes.

Class	Pixel count	Image pixel count	Frequency	Resulting weight
Black background	26 255 602	78 162 629	0.3359	1
Light background	96 827 755	137 304 694	0.7052	0.4763
Crystal	14 221 337	137 007 498	0.1038	3.2361

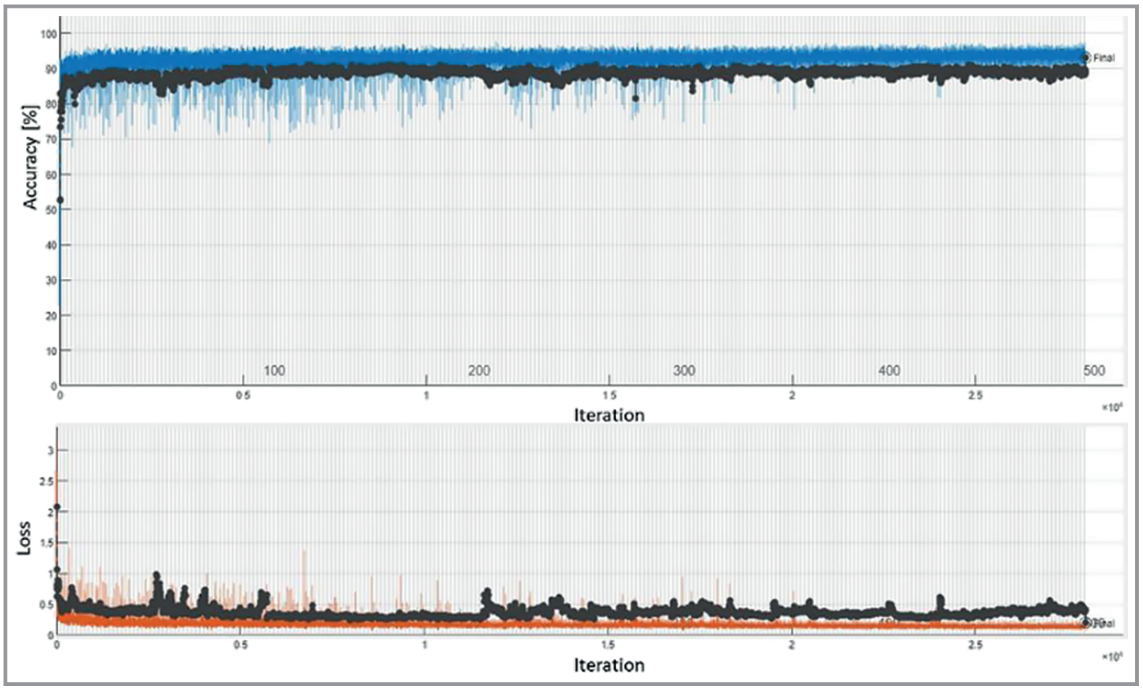

Figure 3. Training course of the Network ResNet-50 with a training duration of 500 epochs and 8 images per mini batch.

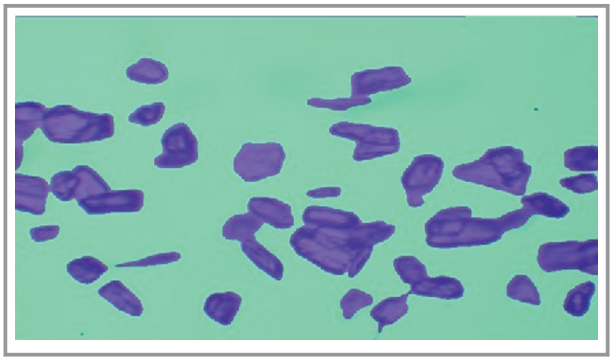

Figure 4. Image classified by ResNet-50 network trained with the settings described in Sect. 3.2. The image is cut to the relevant parts to reduce computational effort. Bright blue color indicates a "light background" whereas the dark blue color indicates the class "crystals".

dicates a "light background" whereas the dark blue color indicates the class "crystals". The third class, "dark background" is not found in this cropped image section. As seen in Fig. 4 the crystals are clearly recognized separately from the light background. Even though the training of the CNN has been designed to reduce the agglomeration of crystals by the CNN, many crystals are still recognized as a big agglomerate. To improve the result, a post-processing algorithm is developed and applied to the image in the following section.

3.4 Results of the Applied Post-Processing Steps

Feature extraction is performed a posteriori, thus after applying a series of post-processing or thresholding methods, which are described in the following. After the original image (Fig. 5a) has passed the CNN, resulting in Fig. 5b, the image is first converted into a binary image (Fig. 5c). Via a watershed algorithm and morphological operations, the final image is obtained (Fig. 5d).

The mask obtained by the CNN (Fig. 5b) is binarized so that only white and black pixels are visible (Fig. 5c) The image is binarized by setting all pixels marked as crystals as true (white) and all other pixels as false (black). To neglect wrongfully detected crystals, a few morphological operations are applied. First, every pixel space below 20 px^2 (equals $6.5 \times 6.5\,\mu m^2$) was deleted. Objects with a diameter below 6.5 µm are thus sorted out. Second, morphological closing using a two-pixel sized disc element is performed. Additionally, holes are closed and crystal patches at the border are deleted, as they are cut off and therefore falsify the result. As seen in Fig. 5c to 5d, some crystals, mostly former agglomerates, are separated by using watershed algorithm. The watershed transform finds "watershed ridge lines" in an image by treating it as a surface where light pixels represent high elevations and dark pixels represent low elevations. The watershed transform can be used to segment contiguous regions of interest into distinct objects [29].

To finally neglect the agglomerates of *L*-alanine, crystal patches outside a circularity range of 85–95 % are negated. This sorting is based on the assumption that crystals usually

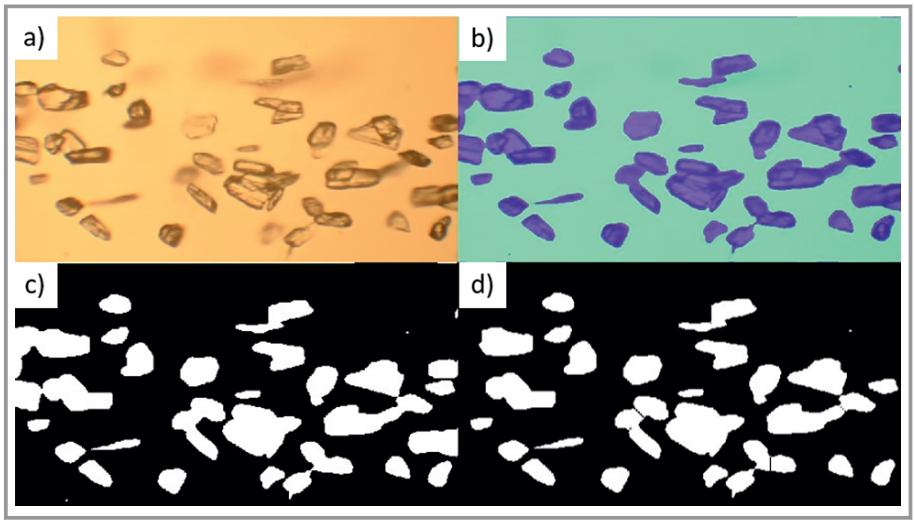

Figure 5. Image classified by ResNet-50 network trained with the settings described above. The image is cut to the relevant parts to reduce computational effort. After the original image (a) passed the CNN, resulting in b), the image is converted into a binary image (c). Via a watershed algorithm and morphological operations, the final image is obtained (d).

have a round or cubic shape instead of the branched and complicated shape of an agglomerate [30]. This decision led to a significant improvement in the results. The first horizontal line of pixels also contains some areas wrongfully detected as crystals, which are deleted due to this circularity threshold. This adjustable parameter might have to be changed when another type of crystals is evaluated.

4 Results and Discussion

The first set of the final test data set persists of 162 images, containing crystals sieved in a range from 125 to 180 µm, the crystals in the second image data set consisting of 323 images range from 90 to 125 µm. The exact same image data is evaluated by the approach of Schmalenberg et al. and the AI-based algorithm. With the classifications of the CNN, the crystals are divided into 10 µm wide classes. A Q_3 distribution is then created from these classes. For the experimental data, the largest crystal of each 10 µm interval is marked.

The calculated Q_3 distribution of the sieved *L*-alanine fractions of 125–180 µm is displayed over all values in Fig. 6. The PSD obtained by AI evaluation shows an unusual increase in the classes from 50 to 110 µm even though the premeasured range is from 125 to 180 µm. This increase has two origins. First, objects between 50 and 110 µm are most likely to be inside the accepted circularity range. The discrepancy can be explained by the measuring of the circularity. The circularity is computed by dividing the measured diameter and the diameter of the area equivalent circle. For example, for very small objects the circularity therefore might even transcend one. The occurrence of this effect decreases with an increasing diameter, but still has a small impact. The second reason is found in the watershed algorithm. The watershed algorithm splits agglomerates and aggregates in the binarized image (as seen in the lower right image of Fig. 4). Multiple crystals are detected as one agglomerate or aggregate, because they partially overlap on the image, since the image covers only two dimensions. Therefore, the overlapping area of two crystals can only be accounted to one of those crystals or even more likely, the overlapping area is divided to the two crystals. Both crystals appear smaller than they are. Since the original PSD measured by sedimentation analysis is given between 125 and 180 µm, crystals received through the watershed algorithm are found in the particle classes below the actual PSD.

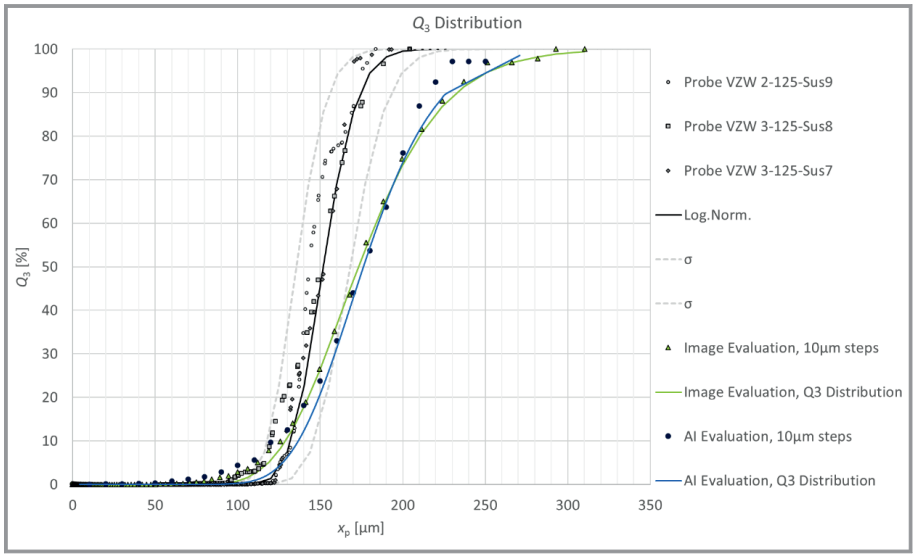

Figure 6. Q_3 distribution of the sieving fraction 125–180 µm estimated by the network described above compared to the results presented by Schmalenberg et al. [13]. The blue line is the estimated Q_3 distribution, evaluated via AI. Green marks the results from the image analysis proposal by Schmalenberg et al., the black line marks the results by the sedimentation analysis. The shapes mark the biggest particle of every 10 µm class of the corresponding color.

The overall results of the AI-based evaluation lie close to the results of the image analysis proposal by Schmalenberg et al. [13]. Yet, the largest found size of the AI-based evaluation was 230 µm, whereas the routine developed by Schmalenberg et al. found the largest crystal at 310 µm. Furthermore, it should be noted that sedimentation experiments favor a shift of the PSD to the smaller side. This fact can be explained by the measurement method of sedimentation analysis. Smaller particles fall less quickly than larger particles and are thus in the detection window for a considerably longer time. To further evaluate the results a comparison with two other methods over the same batch of crystals is given. For the given sieved fraction between 125 and 180 µm sedimentation analysis works well, while the image analysis approaches seem to present the results larger than they are.

The second evaluated sieve fraction (90–125 µm) is shown in Fig. 7. As can be seen with the comparison of different measures, a satisfactory PSD can be developed over the images evaluated by the CNN. However, a stretching of the curve to the right can be seen as some found crystal diameters are above 125 µm. This stretching can also be seen in the evaluation of Schmalenberg et al. The evaluation with CNN shows good results in the middle and especially in the high size ranges, which are clearly below the results of Schmalenberg et al. [12, 13, 20] On the other hand, the evaluation with CNN in the low value ranges of the PSD is far from the results of the sedimentation analysis. This can be explained by the effects of watershed and roundness described above.

5 Conclusion and Outlook

This work investigated the analysis of images containing crystals using a convolutional neural network. The CNN was trained to be able to recognize the crystals on the images. In the next step, a particle size distribution was generated from the recognized crystals. To evaluate the results, the generated PSD is compared to a PSD obtained using sedimentary analysis as well as with a previously developed image analysis routine [13].

To evaluate the classification performed by the presented CNN, it is tested on two sets of images, containing a previously determined particle fraction. The first set persists of images, containing crystals sieved in a range from 90 to 125 µm, the crystals in the second set range from 125 to 180 µm. With the classifications of the CNN, a Q_3 distribution is calculated. The particles were divided into subclasses of 10 µm width with the diameter of the biggest particle of every class plotted with the cumulated share of the total volume of the class. With a log-normal distribution an estimated Q_3 distribution was fit to those values.

In the future, more differently illuminated images and crystal types should be evaluated. By including them in the training data, accuracy of the CNN might increase further. Furthermore, it will be also tested whether CNN-based image analysis can be applied to three-dimensional micro-computed images of the crystals to obtain 3D shape and volumetric information.

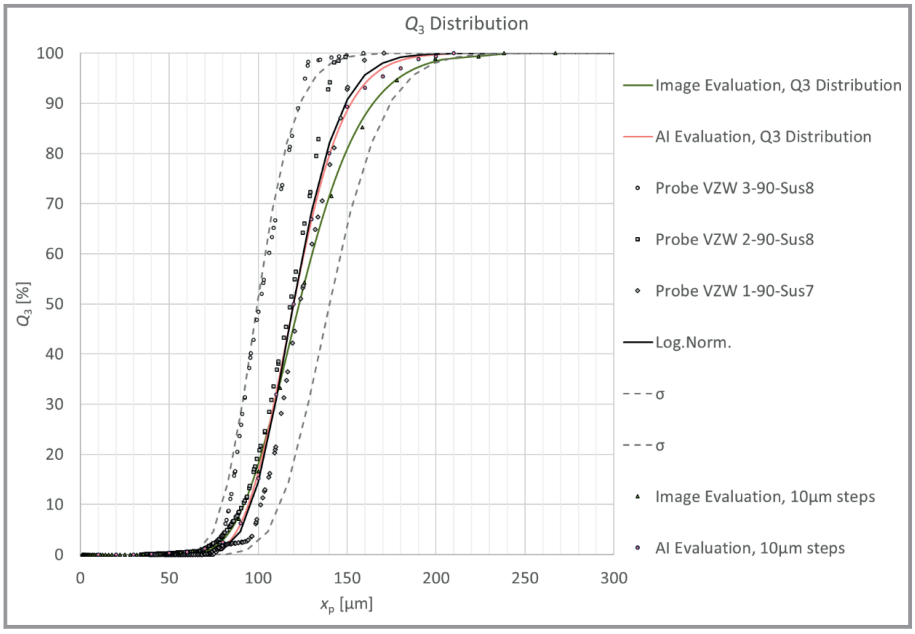

Figure 7. Q_3 distribution of the sieving fraction 90–125 µm estimated by the network described above compared to the results presented by Schmalenberg et al. The red line is the estimated Q_3 distribution, evaluated via AI. Green marks the results from the image analysis proposal by Schmalenberg et al., the black line marks the results by the sedimentation analysis. The shapes mark the biggest particle of every 10 µm class of the corresponding color.

Acknowledgments

The BMWK is acknowledged for funding this KEEN project initiative (Support code: 01MK20014S). The authors want to thank Carsten Schrömges and the glass manufacturing workshop. Open access funding enabled and organized by Projekt DEAL.

Sub- and Superscripts

circ	circular
n	negative
p	positive

Abbreviations

AI	Artificial Intelligence
ANN	Artificial Neural Network
CNN	Convolutional Neural Network
DL	Deep Learning
FEP	Fluorinated ethylene-propylene
LND	Logarithmic normal distribution
ML	Machine Learning
PSD	Particle Size Distribution
ROI	Region of Interest

References

[1] Z. K. Nagy, G. Fevotte, H. Kramer, L. L. Simon, *Chem. Eng. Res. Des.* **2013**, *91 (10)*, 1903–1922. DOI: https://doi.org/10.1016/j.cherd.2013.07.018

[2] H. Lorenz, J. Ulrich, *Chem. Ing. Tech.* **2011**, *83 (12)*, 2089–2092. DOI: https://doi.org/10.1002/cite.201100117

[3] L. Bittorf, F. Reichmann, M. Schmalenberg, S. Soboll, N. Kockmann, *Chem. Eng. Technol.* **2019**, *42 (10)*, 1985–1995. DOI: https://doi.org/10.1002/ceat.201900120

[4] J. Emmerich, Q. Tang, Y. Wang, P. Neubauer, S. Junne, S. Maaß, *Chin. J. Chem. Eng.* **2019**, *27 (2)*, 257–277. DOI: https://doi.org/10.1016/j.cjche.2018.11.011

[5] F. M. Etzler, M. S. Sanderson, *Part. Part. Syst. Charact.* **1995**, *12 (5)*, 217–224. DOI: https://doi.org/10.1002/ppsc.19950120503

[6] G. Eshel, G. J. Levy, U. Mingelgrin, M. J. Singer, *Soil Sci. Soc. Am. J.* **2004**, *68 (3)*, 736–743. DOI: https://doi.org/10.2136/sssaj2004.7360

[7] A. Dobrowolski, R. Strob, J. F. Dräger-Gillessen, D. Pieloth, G. Schaldach, H. Wiggers, M. Thommes, *Int. J. Pharm.* **2019**, *567*, 118501. DOI: https://doi.org/10.1016/j.ijpharm.2019.118501

[8] C. F. Mora, A. K. H. Kwan, H. C. Chan, *Cem. Concr. Res.* **1998**, *28 (6)*, 921–932. DOI: https://doi.org/10.1016/S0008-8846(98)00043-X

[9] C. Igathinathane, L. O. Pordesimo, E. P. Columbus, W. D. Batchelor, S. Sokhansanj, *Comput. Electron. Agric.* **2009**, *66 (2)*, 147–158. DOI: https://doi.org/10.1016/j.compag.2009.01.005

[10] H. Li, J. Li, J. Bodycomb, G. S. Patience, *Can. J. Chem. Eng.* **2019**, *97 (7)*, 1974–1981. DOI: https://doi.org/10.1002/cjce.23480

[11] S. Shirmohammadi, A. Ferrero, *IEEE Instrum. Meas. Mag.* **2014**, *17 (3)*, 41–47. DOI: https://doi.org/10.1109/MIM.2014.6825388

[12] M. Schmalenberg, F. Sallamon, N. Kockmann, *Chem. Ing. Tech.* **2018**, *90 (9)*, 1319. DOI: https://doi.org/10.1002/cite.201855404

[13] M. Schmalenberg, F. Sallamon, C. Haas, N. Kockmann, in *Proc. of the ASME 18th International Conference on Nanochannels, Microchannels, and Minichannels*, The American Society of Mechanical Engineers. New York **2020**.

[14] C. Borchert, K. Sundmacher, *Chem. Eng. Technol.* **2011**, *34 (4)*, 545–556. DOI: https://doi.org/10.1002/ceat.201000465

[15] Y. Huo, T. Liu, H. Liu, C. Y. Ma, X. Z. Wang, *Chem. Eng. Sci.* **2016**, *148*, 126–139. DOI: https://doi.org/10.1016/j.ces.2016.03.039

[16] M. Schmalenberg, L. Hohmann, N. Kockmann, in *Proc. of the ASME 16th International Conference on Nanochannels, Microchannels, and Minichannels 2018*, The American Society of Mechanical Engineers. New York **2018**.

[17] G. Wypych, *Handbook of Polymers*, ChemTec Publishing, Toronto **2016**.

[18] R. Budwig, *Exp. Fluids* **1994**, *17 (5)*, 350–355. DOI: https://doi.org/10.1007/BF01874416

[19] L. Hohmann, M. Schmalenberg, M. Prasanna, M. Matuschek, N. Kockmann, *Chem. Eng. J.* **2019**, *360*, 1371–1389. DOI: https://doi.org/10.1016/j.cej.2018.10.166

[20] M. Schmalenberg, S. Kreis, L. K. Weick, C. Haas, F. Sallamon, N. Kockmann, *Processes* **2021**, *9 (9)*, 1537. DOI: https://doi.org/10.3390/pr9091537

[21] L. M. Neuendorf, F. Z. Baygi, P. Kolloch, N. Kockmann, *ACS Eng. Au* **2022**, *2 (4)*, 369–377. DOI: https://doi.org/10.1021/acsengineeringau.2c00014

[22] O. S. Bayomie, R. F. L. de Cerqueira, L. Neuendorf, I. Kornijez, S. Kieling, T. H. Sandermann, K. Lammers, N. Kockmann, *Comput. Chem. Eng.* **2022**, *164*, 107904. DOI: https://doi.org/10.1016/j.compchemeng.2022.107904

[23] D. Kossmann, T. Wilhelm, G. A. Fink, in *Proc. 2020 25th International Conference on Pattern Recognition (ICPR)*, IEEE, Piscataway, NJ **2020**.

[24] M. E. Taylor, P. Stone, *J. Mach. Learn. Res.* **2009**, *10 (56)*, 1633–1685.

[25] M. Stiess, *Mechanische Verfahrenstechnik: Partikeltechnologie*, 3rd ed., Springer-Lehrbuch, Springer, Heidelberg **2009**.

[26] F. Podczeck, *Powder Technol.* **1997**, *93 (1)*, 47–53. DOI: https://doi.org/10.1016/s0032-5910(97)03257-9

[27] C. Shorten, T. M. Khoshgoftaar, *J. Big Data* **2019**, *6 (1)*, 60. DOI: https://doi.org/10.1186/s40537-019-0197-0

[28] Y. Han, G. Roig, G. Geiger, T. Poggio, *Sci. Rep.* **2020**, *10 (1)*, 1411. DOI: https://doi.org/10.1038/s41598-019-57261-6

[29] www.mathworks.com/help/images/ref/watershed.html (Accessed on December 11, 2022)

[30] M. Senechal, in *Symmetry: Unifying Human Understanding* (Ed: I. Hargittai), Pergamon Press, New York **1986**. DOI: https://doi.org/10.1016/B978-0-08-033986-3.50042-2

